This document is the Accepted Manuscript version of a Published Work that appeared in final form in ***Macromolecules*** 53(5) : 1585-1595 (2020), copyright © 2020 American Chemical Society after peer review and technical editing by the publisher. To access the final edited and published work see https://doi.org/10.1021/acs.macromol.9b02473

Synthesis, Structure and Crystallization Behavior of Amphiphilic Hetero-arm Molecular Brushes with Crystallizable Poly(ethylene oxide) and *N*-Alkyl Side Chains

Elaine Barnard[†], *Rueben Pfukwa*[†*], *Jon Maiz*[‡], *Alejandro J. Müller*[‡,‖*] *and Bert Klumperman*[†*]

[†]Department of Chemistry and Polymer Science, Stellenbosch University, Private Bag X1, Matieland 7602, South Africa

[‡] POLYMAT and Polymer Science and Technology Department, Faculty of Chemistry, University of the Basque Country UPV/EHU, Paseo Manuel de Lardizábal, 3, 20018 Donostia-San Sebastián, Spain.

‖ IKERBASQUE, Basque Foundation for Science, Bilbao, Spain.

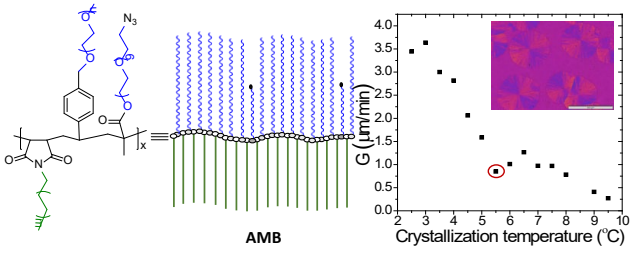

For Table of Contents use only

ABSTRACT: A series of hetero-arm amphiphilic molecular brushes (AMBs) with poly(ethylene glycol) (PEG) and long chain *n*-alkyl side chains were synthesized via conventional free radical polymerization (FRP) of mainly 4-vinyl benzyl-PEG methyl ether and *N*-alkylmaleimide macromonomers. By varying PEG side chain degree of polymerization (D.P. = 12, 16 and 20) and *n*-alkyl chain lengths (C_{16} and C_{20}), AMBs with varying combinations of side chain lengths were produced. This enabled the elucidation of the effect of side chain length on AMB phase behavior, semicrystalline morphologies and crystallization kinetics, via differential scanning calorimetry, polarized light optical microscopy and x-ray diffraction experiments. Calculations of segregation strength together with SAXS measurements indicate that all materials are probably phase segregated structure in the melt. Most of the AMB materials prepared were double crystalline, i.e., contained crystals from alkyl and PEG chains. AMB crystallization was constrained by AMB architecture, the frustration being most evident in AMBs with combinations of either low $D.P._{PEG}$, or short alkyl chain lengths. Large, well-developed spherulites, implying break-out crystallization from a weakly segregated melt, were only observed for the AMBs with the combination of the longest PEG chain (D.P. = 20) and longest alkyl chain length (C_{20}). A peculiar behavior was found when spherulitic growth rates and overall crystallization rates of the PEG chains, within this particular AMB sample, were determined as a function of crystallization temperature. In both cases, a distinct minimum with decreasing temperature was observed, probably caused by the challenges encountered in crystal packing of the PEG side chains, tethered to an amorphous backbone, which also contained already crystallized C_{20} chains. This minimum is analogous to that observed in the crystallization of long chain *n*-alkanes, or high molar mass polyethylenes with bromine pendant groups that has been attributed to a self-poisoning effect; this is the first observation of this phenomenon in AMBs.

Keywords: amphiphilic molecular brushes, double crystalline materials, PEG self-poisoning, PEG side chains, alkyl side chains.

INTRODUCTION

The fabrication of functional nanomaterials, in the solution or solid-state is important for photonics,[1] lithography,[2] electronics,[3] drug delivery,[4,5,6] and sensors.[7,8] Ongoing research focuses on controlling morphology, domain sizes, patterns, and functionality in order to access desired properties, functions and improved performance. Molecular brushes (MBs), i.e., graft copolymers with a backbone and side chains, are interesting macromolecular building blocks for nanomaterial fabrication.[9,10] MBs are amenable to either melt[11,12] or solution[13,14] self-assembly, and can also undergo single-chain folding,[15] creating well-defined nanomaterials. MB properties can be adjusted by varying the grafting density, backbone flexibility or rigidity,[16,17] side chain length, and side chain chemistry,[18,19,20,21] with either homo- or heterografts.[22] In densely grafted MBs, high steric crowding results in stiff and extended backbones, decreasing chain entanglements, significantly reducing viscosities, and in hetero-MBs this can result in faster ordering.[12,23] Hetero-MBs can be accessed by "grafting from" a backbone with different initiator functionalities, e.g., OH/Br, via different polymerization mechanisms, e.g., ring-opening polymerization (from OH) or an atom transfer radical polymerization (from Br).[21,24] Alternatively hetero-MBs can be accessed by copolymerizing macromers with different side chains, i.e., "grafting through",[22,25,26,27,28] resulting in statistical,[27] gradient[22,26] or alternating hetero-MBs, depending on macromers reactivity.[25,29]

Hetero-MBs with crystallizable side chains are intriguing materials, the combination of different crystal structures can influence the morphology and properties of the heterobrush copolymer in the solid, and solution state, hence such materials are very useful scaffolds for the facile preparation of nanostructured materials.[22,30] The crystallization behavior has been shown to depend on the nature of the backbone, i.e., flexible, semi-rigid or rigid, the grafting densities of the side chains and the side chain lengths.[16] Side chain crystallization, however, is frustrated by their dense anchoring to a polymer backbone,[9,16] which constrains the ordering of the crystallizable side chains, and the manner in which the chains are integrated into growing crystals.[31]

Studies on the effect of the configurational constraints, placed by the hetero-MB architecture, on crystallization kinetics, and ultimately morphology, however, are still limited. Herein, we took an in-depth look at amphiphilic hetero-MBs (AMBs) with an amorphous main chain and two different crystallizable side chains, i.e., poly(ethylene glycol) (PEG) and *n*-alkyl moieties. AMB side chain length combinations were systematically varied and the effect on crystallization kinetics and morphology investigated. The AMBs were prepared by the *grafting through* approach, via conventional free radical terpolymerization of macromonomers containing either PEG or alkyl chains of different lengths, i.e., polar 4-vinyl benzyl-PEG methyl ethers (VB-PEG), *tert*-butyl diphenyl silyl poly(ethylene glycol) methacrylate (TBDPSi-PEGMA), and apolar *N*-alkyl maleimides (MI-C_m), see Scheme 1.

PEGMA incorporation, which was kept at ≤ 10%, is in light of a concurrent solution-state self-assembly study based on the same AMBs. Side chain crystallization was strongly influenced by side chain lengths, and possibly backbone rigidity, presumably due to frustration in the crystalline packing, caused by the brush architecture, as evidenced by differential scanning calorimetry (DSC) and X-ray diffraction (XRD) studies. Intriguingly, measurements of spherulitic

growth rates (by Polarized Light Optical Microscopy, PLOM) and overall crystallization rate (by DSC) revealed an unusual minimum with increasing undercooling, reminiscent of the self-poisoning phenomenon observed in long chain *n*-alkanes, or high molar mass polyethylenes with bromine pendant groups.[32,33,34]

Scheme 1. Synthetic procedure for preparing hAMBs with varying side chain lengths.

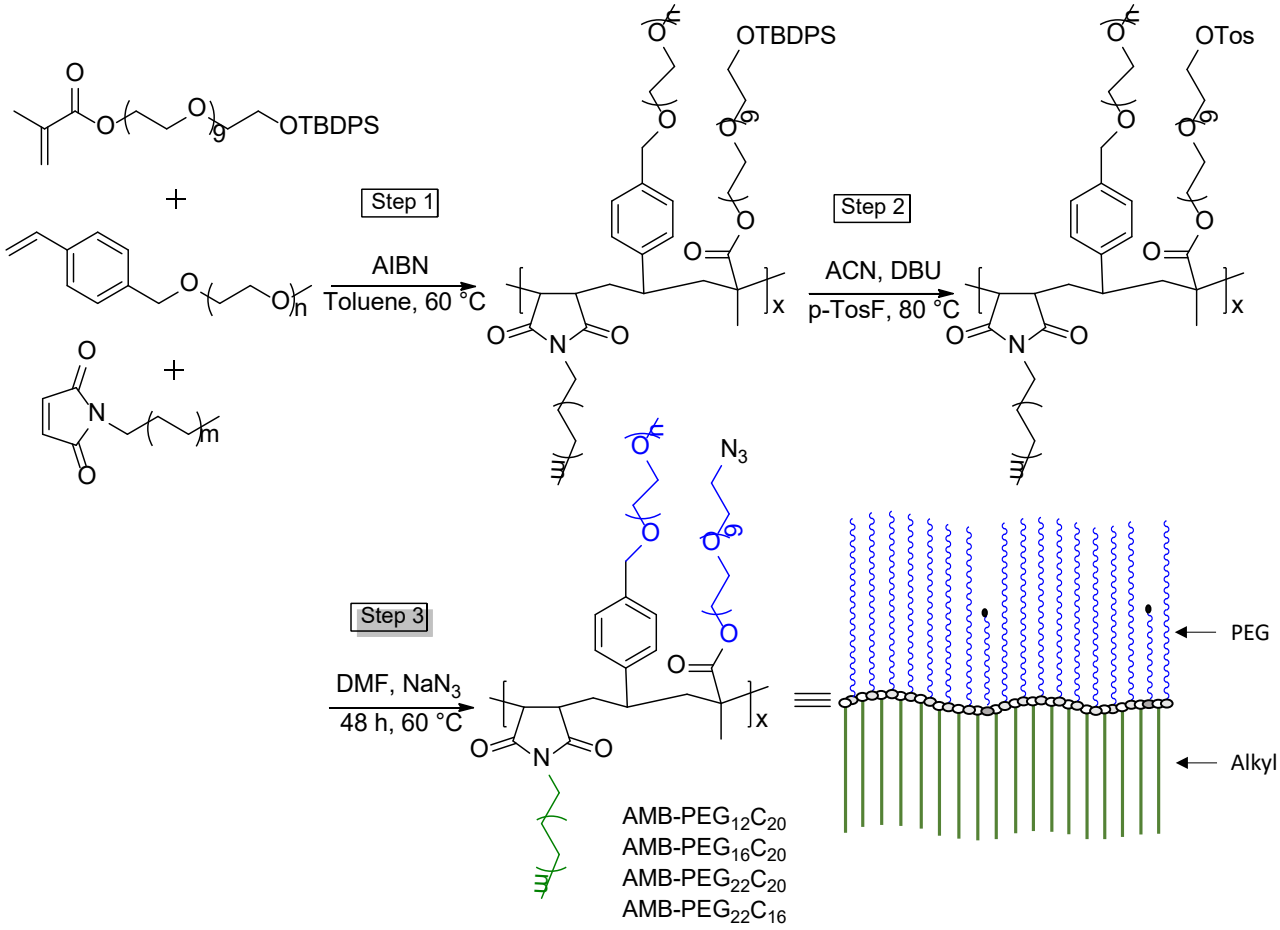

EXPERIMENTAL SECTION

Materials.

Poly(ethylene glycol) mono methyl ethers (PEG, M_n ~ 550 g/mol, M_n ~750 g/mol and M_n ~1000 g/mol, Sigma Aldrich) were azeotropically dried in toluene to remove water. Sodium

hydride (60% dispersion in mineral oil), 4-vinylbenzyl chloride (90%), 1-bromooctane (99%), 1-bromodecane (98%), 1-bromododecane (97%), 1-bromohexadecane (97%), 1-bromoeicosane (≥97%) and poly(ethylene glycol)$_{10}$ methacrylate were purchased from Sigma-Aldrich and used without further purification. 2,2'-Azobisisobutyronitrile (AIBN, Sigma Aldrich) was recrystallized from methanol and dried under vacuum. Tetrahydrofuran (THF) and toluene were purified by stirring over NaOH, followed by distilling from sodium/benzophenone, and stored over molecular sieves. All anhydrous solvents were bought from Sigma-Aldrich.

Methods.

^{1}H nuclear magnetic resonance (NMR) spectroscopy

^{1}H nuclear magnetic resonance (NMR) spectroscopy was performed on a Varian 300 MHz VNMRS NMR instrument or a Varian 400 MHz UNITY INOVA NMR instrument equipped with a Varian magnet (7.0 T). Depending on the solubility of the synthesized compounds various deuterated solvents were used including, deuterated chloroform ($CDCl_3$), deuterated *N*,*N*-dimethylformamide (DMF-d_7), and deuterated dimethyl sulfoxide (DMSO-d_6).

Differential Scanning Calorimetry

A Perkin Elmer Pyris DSC 8500 was used for non-isothermal and isothermal crystallization measurements and all DSC scans were analyzed using Pyris Manager Software. Temperature and enthalpy were calibrated with indium and tin standards. The sample weight was ~3 mg in all cases. For the non-isothermal DSC analyses, the samples were melted in the DSC for 3 min at 70 °C to erase any previous thermal history. The samples were then cooled at 20 °C·min^{-1} from 70 to −50 °C, held there for 1 min and then heated at the same rate from −50 to 70 °C. The second heating scan was employed as data in this work.

Some of the samples, as will be shown below, exhibited two well separated crystallization exotherms upon cooling from the melt. The highest temperature crystallization peak corresponded to the crystallization of the alkyl side chains, while the low temperature peak was due to the crystallization of the PEG chains.

Attempts were made to investigate the isothermal crystallization behavior of the first exothermal peak (alkyl SC crystallization), but analyses were not successful since the alkyl SCs crystallization and melting temperatures were too close to each other, making accurate isothermal crystallization measurements impossible.

Isothermal crystallization was therefore only employed to investigate the second exothermal peaks formed by the crystallization of the PEG side chains, after the alkyl chains had been crystallized.

Isothermal protocol 1a: samples were heated to 70 °C and kept at this temperature for 3 min to erase the thermal history. The sample was then cooled from the melt at 1 °C/min to 10 °C to ensure complete crystallization of the first exothermal peak is identical for each run. The sample was then further cooled from 10 °C at 50 °C/min to the set crystallization temperature (T_c) and held there for 15 min or longer until saturation was reached. The isothermal crystallization of the sample was then recorded. A high cooling rate of about 50 °C/min was used to minimize non-crystallization of the sample during cooling. Finally, the sample was heated at 20 °C/min in order to record the melting behavior of the isothermally crystallized polymer brush.

Wide-and small-angle X-ray scattering (WAXS/SAXS)

In-situ simultaneous SAXS/WAXS measurements were carried out at the beamline BL11-NCD in the ALBA Synchrotron Radiation Facility (Cerdanyola del Valles, Barcelona, Spain). The

samples were placed in glass capillaries. The temperature profile was controlled by a Linkam Scientific Instruments THMS600 stage coupled to a liquid nitrogen cooling system. The hot-stage was programmed to perform the crystallization and subsequent heating and at the same time register the SAXS/WAXS patterns. The thermal protocol was as follows: heating from room temperature to 70 °C, followed by holding for 3 min at 70 °C. Once the thermal history was erased, the samples were cooled down at 20 °C·min^{-1} to the selected isothermal temperature. After the isothermal step, the samples were heated at a rate of 20 °C·min^{-1}. The energy of the X-ray source was 12.4 keV (λ = 1.0 Å). SAXS scattering patterns were collected using an ADSC Q315r detector with a resolution of 3070 × 3070 pixels (pixel size: 102 μm^2). The sample-to-detector distance was 6388.5 mm, covering a scattering vector q range from 0.2 to 2.5 nm^{-1}. The tilt angle was 0°. WAXS patterns were recorded using a Rayonix LX255-HS detector with a resolution of 1920 × 5760 pixels (pixel size: 40 μm^2). The sample-to-detector distance was 126.8 mm, the effective scattering vector q range was 8-22 nm^{-1}, and the tilt angle 30°. The two-dimensional scattering patterns were integrated radially to one dimensional intensity profiles using the program DAWN, as a function of the inverse scattering vector, $q = 2\pi/d = 4\pi \sin\theta/\lambda$, where λ is the X-ray wavelength (λ = 1.0 Å) and 2θ is the scattering vector. The calibration was performed employing silver behenate (SAXS) and Cr_2O_3 (WAXS) standards.

Polarized Light Optical Microscopy (PLOM)

An OLYMPUS BX51 polarized light optical microscope was used to observe the spherulitic morphologies. A Linkam LNP95 hot stage connected to a liquid nitrogen system was used to control the temperature. The samples were prepared by pressing two glass plates in which a small amount of the sample was sandwiched at 70 °C on a hot stage, subsequently two different isothermal protocols were employed.

Isothermal protocol 1b: samples were heated to 70 °C and kept at this temperature for 3 min to erase the thermal history. Once the samples formed a thin film, they were cooled from the melt at 5 °C/min to 10 °C to ensure complete crystallization of the first exothermal peak is identical for each run. The sample was then further cooled from 10 °C at 50 °C/min to the set crystallization temperature (T_c). The samples were then kept at the crystallization temperature until all the spherulites impinged with each other.

Isothermal protocol 2: samples were heated to 70 °C and kept at this temperature for 3 min to erase the thermal history. Once the samples formed a thin film, a controlled cooling was applied, making sure that the cooling rate was 20 °C·min^{-1}, down to the set isothermal T_c temperature. The samples were then kept at the crystallization temperature until all the spherulites impinged with each other. Micrographs were taken with a Leica DC420 digital camera. The sizes of the growing spherulites were measured by Olympus Stream Essentials software at appropriate intervals of time, and the spherulitic growth rate (G) of the AMB spherulites were calculated from the slopes of the lines obtained by plotting the spherulite radius against time.

Synthetic Procedures.

4-vinyl benzyl-PEG methyl ethers (VB-PEG),[35] and *N*-alkylmaleimides (MI-C_m)[36] were prepared as described in literature.

tert-Butyl diphenyl silyl-PEG$_{10}$ methacrylate macromonomer (TBDPS-PEGMA): A 3-neck round bottom flask was charged with poly(ethylene glycol) methacrylate (3.5 g, 6.65 mmol, 1 eq.), BHT (0.131 g, 0.595 mmol) and dry DCM (20 mL) and cooled to 0 °C. The base, DBU (2 mL, 13.3 mmol 2 eq.) was added slowly followed by dropwise addition of *tert*-butyl diphenyl silyl chloride (3.46 mL, 13.3 mmol, 2 eq.) in DCM (10 mL). The reaction mixture was stirred for a

further 12 hours at room temperature, followed by the addition of 2 M HCl solution (15 mL). After phase separation, the organic layer was washed with saturated $NaHCO_3$ (15 mL) solution and a brine solution (15 mL). The organic layer was dried over $MgSO_4$, filtered and the filtrate concentrated *in vacuo*. The resulting yellow oil was further purified by liquid column chromatography using 80 % EtOAc/hexane as the eluent and flushing the column with acetone to isolate the pure product in 35 % (1.78 g) yield. ^{1}H NMR (300 MHz, $CDCl_3$) δ 7.69 – 7.64 (m, 4H), 7.44 – 7.32 (m, 6H), 6.13 – 6.10 (m, 1H), 5.56 (m, 1H), 4.28 (t, J = 5.0 Hz, 2H), 3.79 (t, J = 5.35 Hz, 2H), 3.75 – 3.69 (m, 2H), 3.67 – 3.59 (m, 34H), 1.93 (s, 3H), 1.03 (s, 9H). 13C (300 MHz, CDCl3) δ 167.4, 135.7, 133.8, 129.7, 127.7, 125.8, 72.5, 70.6, 69.2, 63.9, 63.50, 26.9, 19.3, 18.4. FT-IR (ATR, cm-1): 2860 (aliphatic, -C-H stretching), 1717 (-C=O), 1637 (C=C stretch), 1100 (C-O-C), 740 and 703 (-O-Si-diphenyl).

General procedure for synthesis of AMBs: *N*-hexadecanemaleimide (MI-C_{16}) (0.150 g, 0.467 mmol, 1 eq.), VB-PEG_{22} (0.520 g, 0.467 mmol, 1 eq.), TBDPSi-PEGMA (0.140 g, 0.140 mmol, 0.3 eq.) were first dried, separately, over molecular sieves in a total volume of 3 mL dry toluene before being added to an argon purged 2-necked flask. AIBN (8.8 mg, 0.054 mmol) in 0.30 mL toluene was added to the system and the reaction mixture was purged for 45 minutes before being placed in an oil bath at 60 °C for 5 h. The unmodified AMB-$PEG_{22}C_{16}$ was purified by precipitation from diethyl ether (×2) and methanol (×1).

General procedure for AMB side chain modification (step 1): Unmodified AMB-$PEG_{22}C_{16}$ (0.310 g, 0.056 mmol TBDPSi units) was dissolved in ACN (15 mL) in a dry, 2-neck round bottom flask. 1,8-Diazabicyclo [5.4.0] undec-7-ene (DBU) (1.74 µL, 0.011 mmol, 20 mol %) was added via a pipette and the reaction mixture was purged with argon. Toluene sulfonyl fluoride was dissolved in dry ACN (1 mL) and added to the reaction flask, followed by stirring under reflux for

48 hours. The solvent was removed *in vacuo* and the crude product was used without further purification in the subsequent step. *(Step 2)*: Crude AMB-$PEG_{22}C_{16}$ was dissolved in dry DMF (15 mL) and added to a dry, 2-neck round bottom flask. An excess amount of NaN_3 (0.046 g, 0.700 mmol, 5 eq.) was added and the reaction mixture was heated to 60 °C and stirred for 2 days under an argon atmosphere. In order to remove the residual macromonomers, the raw product was purified via dialysis against an acetone/water mixture (1:1 v/v) for 2 days, and 100 % water for 1 day, followed by freeze-drying. ^{1}H NMR spectra of the macromonomers and AMBs (before and after modification) are shown in Figure S1 and Figure S2 in Supporting Information.

RESULTS AND DISCUSSION

Synthesis of AMBs. The "grafting through" method was employed in the terpolymerization of VB-PEG, TBDPSi-PEGMA and MI-C_m, with systematically varying combinations of $D.P._{PEG}$ side chain and alkyl chain lengths. Polymerizations were carried out in toluene under conventional free-radical polymerization (FRP) conditions using AIBN as a thermal initiator (see Scheme 1, step 1). The molar feed ratios of VB-PEG/MI–C_m/TBDPSi-PEGMA were kept at 1:1:0.3, in order for the composition of the final AMB to consist predominantly of alternating VB-PEG and MI–C_m side chains, with a small fraction of TBDPSi-PEGMA incorporated. Subsequently, the TBDPSi-PEGMA's side chain end-groups were converted into azide functionalities by first converting the silyl ethers into sulfonate esters, before azidization, via a nucleophilic substitution reaction with NaN_3, Scheme 1.[37] SEC derived number average molecular masses (M_n) were high, however, they can only be considered as approximate since they were obtained by SEC calibrated against linear PMMA standards. Molar mass dispersity values ($Đ$) were also high, consistent with the FRP

approach used. Typical ^{1}H NMR spectra of the AMBs, before and after modification of the methacrylate repeat units, are shown in Figure S2. ^{1}H NMR spectra show characteristic resonances for all three of the macromonomer repeat units in the AMB, as well as the disappearance of vinylic signals in the chemical shift region 5 – 6.8 ppm representative of the double bonds of each of the macromonomers, thus confirming the successful brush formation and purification. The composition of the brushes was estimated by ^{1}H NMR spectroscopy, by comparing the integral ratios of respective macromonomer signals, see Figure S3. Incorporation of VB-PEG, MI-C_m and PEGMA was ~50 mol%, ≥40 mol% and ≤10 mol%, respectively. Although we did not characterize the terpolymer microstructure, it is reasonable to assume that the AMBs have a predominantly alternating VB-PEG/MI-C_m character, based on the obtained copolymer composition, the known copolymerization behavior of VB-PEG/MI-C_m derivatives,[38] and also the known terpolymerization behavior of styrene, methyl methacrylate and maleic anhydride.[39] Henceforth the AMB synthesized are referenced based on VB-PEG and MI-C_m macromonomers, e.g. in Table 1, AMB-$PEG_{22}C_{12}$, refers to the AMB with VB-PEG of $D.P._{PEG}$ side chain = 22, and *N*-alkyl side chains with 12 carbon atoms. Due to *grafting through* approach utilized, every backbone repeat unit bears one side chain (SC), therefore, these AMBs are densely grafted.

Table 1. Characterization details of hAMBs prepared herein

Sample name	AMB			$^aM_n \times 10^{-3}$	$Đ$	D.P^b	AMB Composition
	A	B	C	(g/mol)			A/B/C mol % (wt %)
AMB-$PEG_{12}C_{20}$	VB-PEG_{12}	MI-C_{20}	PEG_9MA	88	2.8	171	40/50/10 (53/37/10)
AMB-$PEG_{16}C_{20}$	VB-PEG_{16}	MI-C_{20}	PEG_9MA	96	3.2	163	44.5/52/3.5 (64/33/3)
AMB-$PEG_{22}C_{20}$	VB-PEG_{22}	MI-C_{20}	PEG_9MA	113	1.7	163	40.9/50.5/8.6 (66/27.5/6.5)
AMB-$PEG_{22}C_{16}$	VB-PEG_{22}	MI-C_{16}	PEG_9MA	120	1.9	176	45/52/3 (73/24/3)

[a]Determined by SEC in DMF, calibrated with PMMA standards. [b]Degree of polymerization used for calculation of χN. Calculating DP: VB-PEG_n (A): A units=Mn ×wt%(A)/Mr(A), MI-C_m (B):A units=Mn ×wt%(B)/Mr(B), PEG_9MA (C): C units=Mn ×wt%(C)/Mr(C), DP=A+B+C.

Table 2. Calorimetric Data of AMBs

Sample	wt %		T_c (°C)		T_m (°C)		ΔH_m^n (J/g)[b]		X_c(%)	
	Alkyl	PEG[a]	Alkyl	PEG	Alkyl	PEG	Alkyl	PEG	Alkyl	PEG
AMB-$PEG_{12}C_{20}$	37	63	21.3	-32	33.4	9.1	35	29	14.1	15.4
AMB-$PEG_{16}C_{20}$	33	67	21.9	-18.2	33.5	19.7	39	57	15.8	30.3
AMB-$PEG_{22}C_{20}$	27.5	72.5	25	-12.8	33.5	26.4	47	62	19.0	32.9
AMB-$PEG_{22}C_{16}$	24	76		-19.9		38		61		32.4

[a]Total PEG wt % i.e. VB-PEG_{12} + PEG_9MA

[b]ΔH_m^n - melting enthalpy normalised with respect to PEG or alkyl side chain fraction

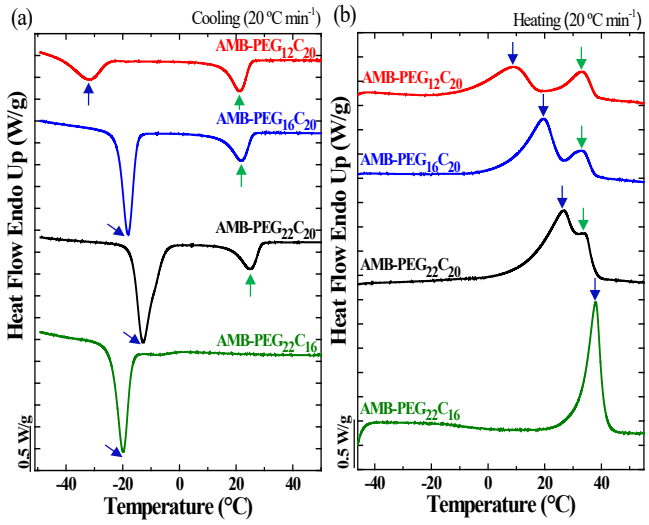

Figure 1. Non-isothermal DSC (a) cooling and (b) subsequent heating scans for AMBs at a scanning rate of 20 °C/min. Green arrow = alkyl side chains, blue arrow = PEG side chains.

Thermal Analysis Using DSC. Figure 1 shows DSC scans obtained during cooling and subsequent heating scans of the AMBs. The DSC traces for AMB-$PEG_{12}C_{20}$, AMB-$PEG_{16}C_{20}$ and AMB-$PEG_{22}C_{20}$ revealed multiple crystallization and melting peaks, indicating that two crystalline phases were formed corresponding to the different pendant arms. Increasing the $D.P._{PEG}$ of the AMBs, with a constant alkyl chain length (i.e. AMB-$PEG_{12}C_{20}$, AMB-$PEG_{16}C_{20}$ and AMB-$PEG_{20}C_{20}$), resulted in an increase in the PEG melting temperature (T_m), crystallization

temperature (T_c) and the normalized melting enthalpies (ΔH_m^n), whilst the calorimetric data for the alkyl side chain remained constant, see Table 2. This shows that increasing the D.P.$_{PEG}$ side chains enhances side chain crystallizability, consistent with literature findings that longer side chains can easily form ordered chain structures.[40,16]

Interestingly, AMB-PEG$_{22}$C$_{16}$ with a shorter alkyl chain length, C$_{16}$, only showed T_m and T_c for the PEG, and not the alkyl side chains. There are two possible reasons for this. Firstly, the presence of two chemically different side chains, with different crystal packing modes can frustrate the packing of the semicrystalline AMB, causing the formation of amorphous alkyl side chains domains,[22] hence longer alkyl chain lengths are required for crystallization to occur. This will be revisited later when we discuss the XRD results. Secondly, it is generally accepted that the backbone and a portion of side chains closest to the backbone do not crystallize, and are incorporated into the amorphous domain surrounding the crystallized side chain portions.[41,22] Additionally, backbone rigidity, and the nature of the linking group, can also influence the length of the side chains' crystallizable portion.[17,16,42,40] More flexible backbones allow for greater conformational adjustments which in turn enable more alkyl –CH_2– groups to enter into the side-chain crystallites.[17] Whilst there is evidence that the size of the chemical junction has an influence on the crystallization behaviour, this is still to be fully rationalised.[16,42]

Our system is based on a rigid, styrene-*alt*-maleimide (SMI) backbone. Compared to the reported, and less rigid poly(styrene-*co*-maleic anhydride)-*g*-1-alcohol (SMA-*g*-C$_n$OH)[40] and poly(methyl vinyl ether-*alt*-maleic anhydride)-*g*-C$_n$ (PVEM-C$_n$),[16] systems, see Figure 2, it is reasonable to expect side chain crystallizability to be more hindered with the more rigid SMI backbone used herein. A combination of these factors, i.e., packing frustrations, backbone rigidity and the linking group could all be at play here, explaining why in poly(styrene-*co*-maleic

anhydride)-*g*-1-alcohol (SMA-*g*-C_nOH)[40], C_{14} side chain is observed to crystallize, whilst in this case C_{16} does not.

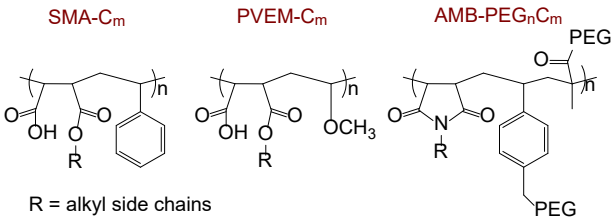

Figure 2. Comparison of MB systems, with different backbones, showing reported SMA-C_m[40] and PVEM-C_m[16] and the AMB-PEG-C_m system used herein.

From the endothermic melting peak, the degrees of PEG and alkyl side chain crystallinity, $X_{c(PEG)}$ and $X_{c(alkyl)}$ respectively, were estimated relative to the heats of fusion for 100 % crystalline PEG (ΔH_m^o= 188.3 J/g[43,44]) and a long chain *n*-alkyl, (eicosane, ΔH_m^o= 247.39 J/g[44]), respectively. $X_{c(PEG)}$ increased with increasing D.P.$_{PEG}$ side chain, see Table 2. Observed X_c values, however, were low, suggesting that only a section of these side chains participate in crystallite formation. Interestingly, comparing the brushes AMB-$PEG_{12}C_{20}$, AMB-$PEG_{16}C_{20}$ and AMB-$PEG_{22}C_{20}$, which have constant C_{20}, the degree of alkyl side chain crystallinity also slightly increased with increasing D.P.$_{PEG}$. This could possibly be explained by the higher $X_{c(PEG)}$ in AMB-$PEG_{22}C_{20}$ compared to AMB-$PEG_{12}C_{20}$ and AMB-$PEG_{16}C_{20}$ which in turn promotes the higher degree of ordering of the alkyl side chains.

Temperature-dependent SAXS/WAXS. The structure of the AMBs was investigated by WAXS experiments performed during cooling from the melt (70 °C to -50 °C) followed by heating from the crystalline state (-50 °C to 70 °C). Figure 3 shows the resulting WAXS patterns during cooling from the melt, followed by heating from the semi-crystalline state. For AMB-$PEG_{12}C_{20}$, AMB-$PEG_{16}C_{20}$ and AMB-$PEG_{22}C_{20}$, the characteristic reflections for both side chains were

detected, whilst for AMB-$PEG_{22}C_{16}$, only the PEG reflections were detected. Therefore, the SAXS results are consistent with the DSC measurements presented above.

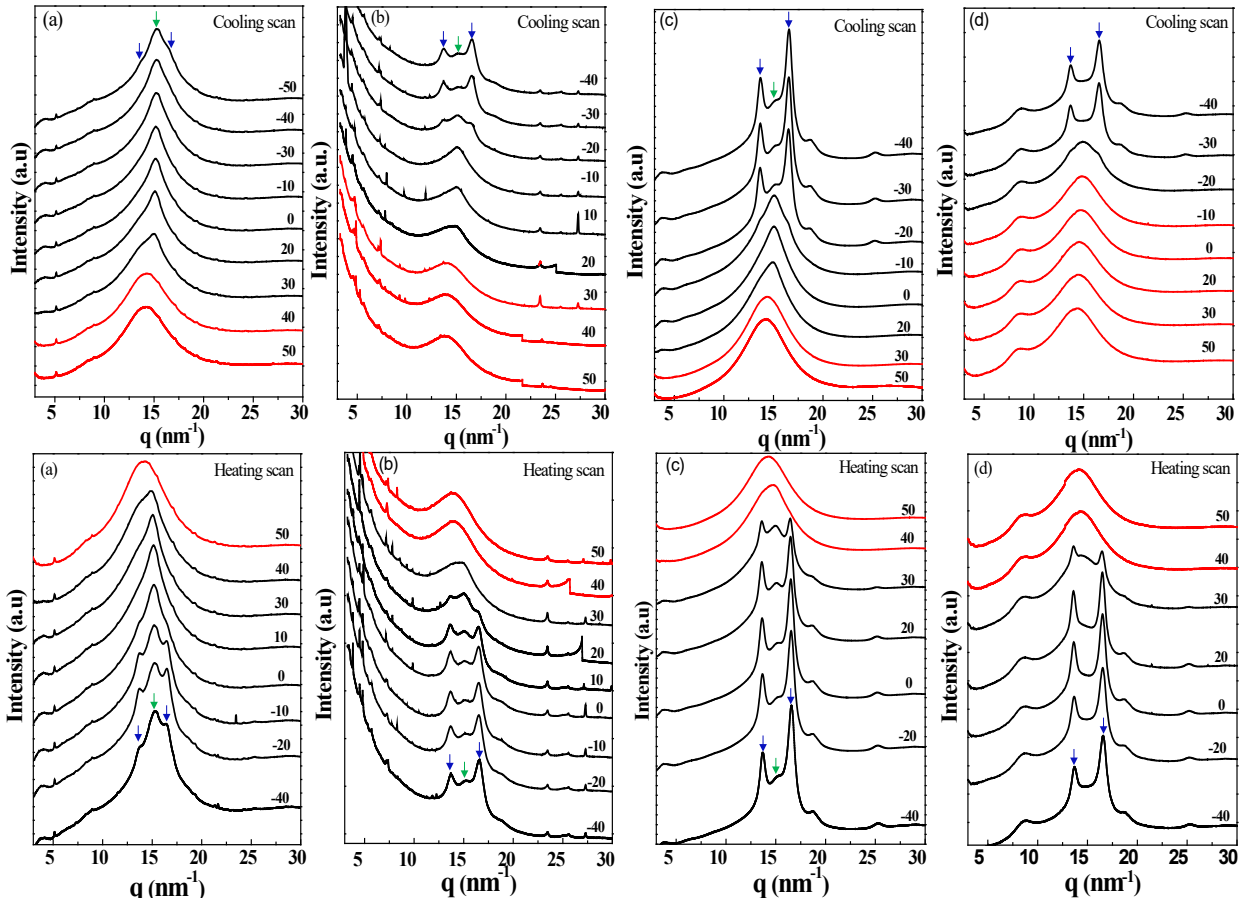

Figure 3. Temperature-dependent WAXS patterns taken during cooling from the melt and heating from the crystalline state of (a) AMB-$PEG_{12}C_{20}$, (b) AMB-$PEG_{16}C_{20}$, (c) AMB-$PEG_{22}C_{20}$ and (d) AMB-$PEG_{22}C_{16}$, respectively. Red WAXS patterns indicate that the AMB is in the melt. Blue arrows indicate PEG crystalline reflections and green arrow indicates the C_{20} crystalline reflection.

The PEG crystalline reflections (blue arrows) are observed at 13.7 and 16.6 nm^{-1} (d = 0.46 and 0.38 nm), corresponding to the (120) and (032) planes, characteristic of the monoclinic cell of PEG with a = 0.805 nm, b = 1.304 nm, c = 1.948 nm, and β = 125.4°.[45,46] The relation of the PEG

reflections intensity also corresponded to D.P.$_{PEG}$. The C_{20} peak (green arrow) is observed at 15.1 nm^{-1}, attributable to a hexagonally packed structure of the *n*-alkyl side chains with an interchain distance of d = 0.42 nm.[47,48,41,22] The reflection observed at 8.65 nm^{-1} in the WAXS pattern of AMB-$PEG_{22}C_{16}$ (see Figure 3d) is likely due to an artifact present in the X-ray analysis instrumentation and not as a result of the crystallization of the polymer. Furthermore, WAXS measurements taken during cooling from the melt also confirmed the crystallization order of the side chains, consistent with DSC results. The C_{20} reflection appeared first during cooling from the melt, followed by the PEG reflections, whilst upon heating the PEG reflections disappeared at lower temperatures than the C_{20}.

In order to get more information on the structural evolution and phase transition behavior of the side chains, analogous temperature-dependent SAXS experiments were conducted. Figure S4 and Figure S5 show the resulting patterns of the full temperature range for the heating and cooling cycles, respectively. AMB-$PEG_{22}C_{20}$ showed the sharpest primary order reflections, followed by AMB-$PEG_{12}C_{20}$, and both AMBs also showed discernible second order reflections, in the temperature range where crystals are present according to WAXS and DSC measurements. The primary scattering of AMB-$PEG_{16}C_{20}$, is evident, but it was very weak, whilst that of AMB-$PEG_{22}C_{16}$ was barely discernible. Both AMBs did not show high order reflections (see Figure S4 (b,d) and Figure S5 (b,d)), suggesting the absence of long-range order. For AMB-$PEG_{22}C_{16}$ the absence of alkyl side chain crystallinity in the brush system likely played a role in the lower crystal ordering, whilst with AMB-$PEG_{16}C_{20}$, the low crystal ordering is probably due to the very high $Đ$, which makes it difficult for optimal lamellar stacking to take place. The morphologies of these two AMBs polymers were difficult to discern and only AMB-$PEG_{22}C_{20}$ and AMB-$PEG_{12}C_{20}$ will be discussed in further detail.

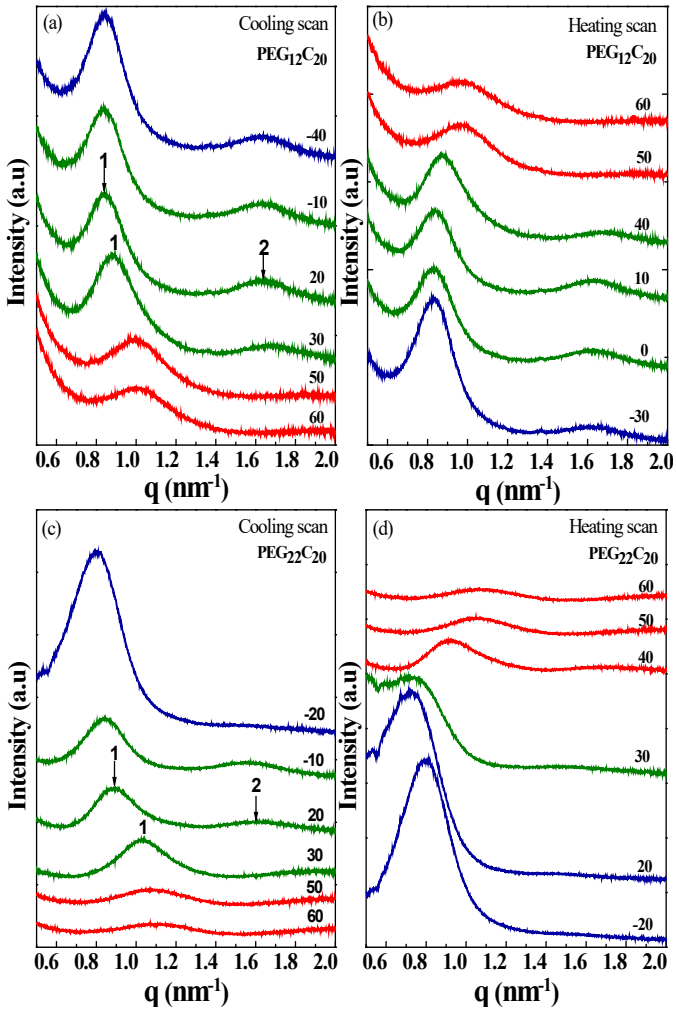

Figure 4. Temperature-dependent SAXS patterns of (top) AMB-$PEG_{12}C_{20}$ and (bottom) AMB-$PEG_{22}C_{20}$ upon cooling from the melt (left), followed by heating from the crystalline state (right). "1" indicates primary peak. Colour indication: Red = AMB is in the melt, green = due to the scattering of alkyl lamellar stacks (i.e., alkyl long period), blue = due to the scattering of both alkyl and PEG lamellar stacks.

From the SAXS patterns of AMB-$PEG_{12}C_{20}$ and AMB-$PEG_{22}C_{20}$ (Figure 4) a change in the primary scattering peaks ("1") can be seen when the temperature decreases from 30 to 20 °C

indicating a shift from the molten (red) to the crystalline state (green = alkyl lamellar stacks, blue = both alkyl and PEG lamellar stacks). For both AMBs, the primary scattering, and its higher order reflection taken at 20 °C, are in the ratio of 1:2, see black arrows, Figure 4a and c, which may be attributed to crystalline lamellar morphology, with a small d-spacing value of 7.52 nm for AMB-$PEG_{12}C_{20}$ and 7.14 nm for AMB-$PEG_{22}C_{20}$.

Looking at AMB-$PEG_{22}C_{20}$, a strong scattering around q = ~0.8 nm^{-1} emerged (Figure 4c and 4d), which may be attributed to the overlap of the diffraction of both alkyl and PEG crystalline lamellar stacks at temperatures below -10 °C. Close inspection of Figure 4c and Figure 5a reveals that after alkyl chain crystallization, the peak further moves to lower q values (higher d* values) when the temperature is lowered and PEG crystallizes. This was confirmed by heating the sample above the melting temperature of the PEG side chains (~26 °C) at which point the peak began to disappear (Figure 4d, green) and the long period (d*) decreased (Figure 5b).

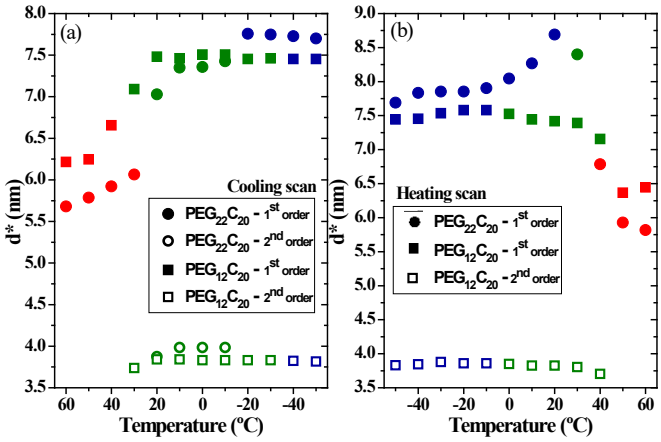

Figure 5. Long period (d*) calculated from SAXS data as a function of temperature during (a) cooling from the melt and (b) heating from the crystalline state. Colour indication: Red = AMB is in the melt, green = due to the scattering of alkyl lamellar stacks (i.e., alkyl long period), blue = due to the scattering of both alkyl and PEG lamellar stacks (i.e., long period of both alkyl and PEG).

At 60 °C, which is far above the melting temperature of both side chain crystallites, broad maxima at scattering vectors of d^* = 5.3 nm (AMB-$PEG_{22}C_{20}$) and 6.0 nm (AMB-$PEG_{12}C_{20}$) can still be seen, suggesting the existence of microphase separated structures in the melt. This is consistent with immiscibility of the hydrophilic PEG and hydrophobic *n*-alkyl side chains and amorphous main chain. After the crystallization of alkyl or PEG components in the samples, the SAXS maxima shift to lower q values (higher d^* values) due to the scattering of the crystalline lamellae formed. The change in maxima position suggests that during crystallization substantial rearrangement of the microphase segregated structures originally present in the melt occurred during crystallization. Most likely, a break-out phenomena where crystallization prevails over phase segregation has occurred, as discussed further below in the PLOM section. Further shown

in Figure 5, the long period values (d^*) seems to be markedly sensitive to these changes occurring during crystallization and subsequent melting of the AMBs.

Although the molecular architecture of the AMBs is completely different from that of well-studied diblock copolymer systems, phase separation for the side chains used herein, is to be anticipated by comparing with a 'block copolymer' equivalent of low molecular weight polyethylene-*block*-PEG.[49] One can get an idea of the segregation strength, i.e., the product of χN (where χ = Flory-Huggins interaction parameter, and N = overall degree of polymerization) for the various corresponding 'blocks', with matching side chain lengths based on the relation $\chi(E/EO) = -0.2802 + 177.4/T$, derived by Sun *et al.*[50,49] The estimated Flory-Huggins interaction parameter was calculated as 0.252 for both samples and the χN parameters for AMB-$PEG_{12}C_{20}$ and AMB-$PEG_{22}C_{20}$ were estimated at 43 and 41, respectively. These values are in the intermediate segregation limit of diblock copolymers typically established for values lower than $\chi N \approx 50$ but larger than 10.[51] We therefore speculate that AMB-$PEG_{12}C_{20}$ and AMB-$PEG_{22}C_{20}$ could undergo microphase segregation in the melt, supporting the observation of SAXS peaks herein. Nevertheless, we have no direct evidence of phase segregation in the melt, apart from the broad SAXS maxima observed. Taking into account that the brush topology could induce a lowering of the segregation strength, which has been calculated for linear diblock copolymers, the possibility that the melt could be homogeneous in these particular brush systems cannot be ruled out.

With the current data at hand, the broad maxima observed in the melt state by SAXS could be due to two possible scenarios: (a) an intermediate phase segregation in the melt, in which case break out crystallization explains the spherulitic morphologies found for one of the samples (see PLOM section below) or (b) a homogeneous melt, where the maximum observed could be due to

compositional fluctuations in the melt attributed to the primary structure or to a hole correlation effect, like the one sometimes observed in melt-mixed diblock copolymers[51]. Both crystallization from either a weak separated melt or a miscible melt would lead to the formation of crystalline lamellae, as clearly observed by SAXS.

Crystalline Morphologies and Growth Kinetics. The crystalline morphologies of the AMBs were investigated using PLOM. Thin films of the polymer brushes were crystallized from the melt at various extents of supercooling. It was, however, only possible to observe spherulites for AMB-$PEG_{22}C_{20}$ (see Figure 6a), which had the combination of the highest $D.P._{PEG}$ and longest alkyl chain lengths used in this study. The spherulites displayed a Maltese cross extinction pattern and are clearly negative (as indicated by the yellow first and third quadrants, and second and fourth blue quadrants, when observed with a red tint plate, as in Figure 6a).

The spherulites are formed by the PEG SCs after the crystallization of the alkyl SCs. Recalling the composition of the AMB-$PEG_{22}C_{20}$ (see Table 2) sample; the AMB consists of 72.5 wt% PEG and only 27.5 wt% of C_{20} alkyl chains. From this 27.5% alkyl chains, only 19% can crystallize during non-isothermal cooling. It is therefore feasible that during isothermal crystallization, only approximately 20% of the alkyl chains can crystallize (less than 6% of the total material in the sample). As a result, small crystallized regions of alkyl chains covalently bonded to the backbone will be present when PEG crystallizes. PEG is however the major component in the sample and the observation of spherulites in these materials indicates that PEG crystallization overcame the phase segregation of the material in the melt and caused a break-out phenomenon or simply formed spherulites from a mixed melt. Break-out is well-known for diblock copolymers with a weak or medium segregation strengths.[52,53] However, both crystallization from either a weak separated melt or a miscible melt could explain the formation of spherulites.

In brushes with lower $D.P._{PEG}$ or shorter alkyl chain length combinations, no superstructural aggregates were observed at the micron scale at least (the optical resolution of PLOM is limited by the wavelength of light at around 400 nm). This would indicate that they formed crystalline superstructures with sizes lower than 0.5 μm during their break-out crystallization or remained micro-phase segregated.

The radial growth rate of the AMB-$PEG_{22}C_{20}$ spherulites, as a function of crystallization temperature T_c, from 2.5 to 9.5 °C, was measured. The spherulitic radius increased linearly (see Figure 6b, enlarged plot is shown in Figure S6 for clarity) with time and the growth rate (G) remained constant during isothermal crystallization until growth was stopped by impingement.

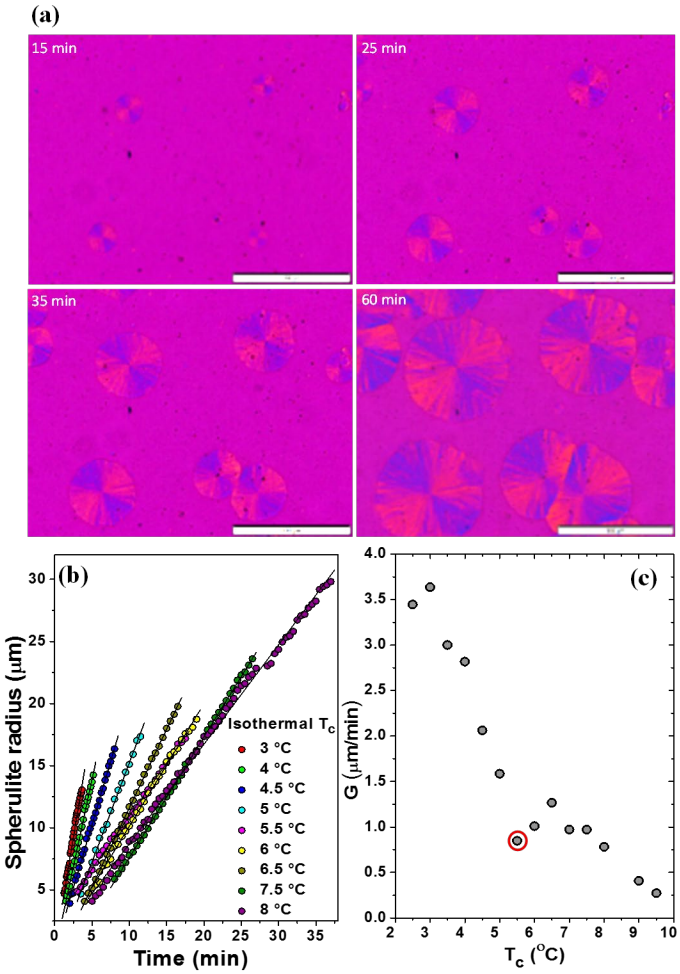

Figure 6. (a) Polarized light optical micrographs showing spherulites growth of AMB-PEG$_{22}$C$_{20}$ at 8 °C. Sample heated to 70 °C and cooled to T_c = 8 °C, at a rate of 20 °C·min^{-1}. Numbers indicate the crystallization time. Scale bar = 100 μm. (b) Spherulite radius versus isothermal crystallization time, at various isothermal temperatures. (c) Linear growth rate, G, of spherulites of AMB-PEG$_{22}$C$_{20}$ as a function T_c, measured by PLOM. Isothermal protocol 2: Cooling from the melt at 20 °C·min^{-1} to the established crystallization temperature

The plot of the experimentally determined spherulitic growth rates (G) as a function of T_c is shown in Figure 6c. The gradient of the growth rate first displayed the expected increase in G with increasing supercooling, before passing through a maximum, followed by a dip into a minimum, the growth rate at 5.5 °C decreasing by ~40 % to the value at 6.5 °C, before it rapidly increased again with further decrease in temperature. The minimum in G was reproduced via PLOM with isothermal protocol 1b, by cooling the sample from the melt at 5 °C·min^{-1}, to 10 °C, to ensure alkyl side chain crystallization, and before cooling further from 10 °C, at 50 °C·min^{-1}. The minimum in G was still observed with decreasing crystallization temperature, see Figure 7a.

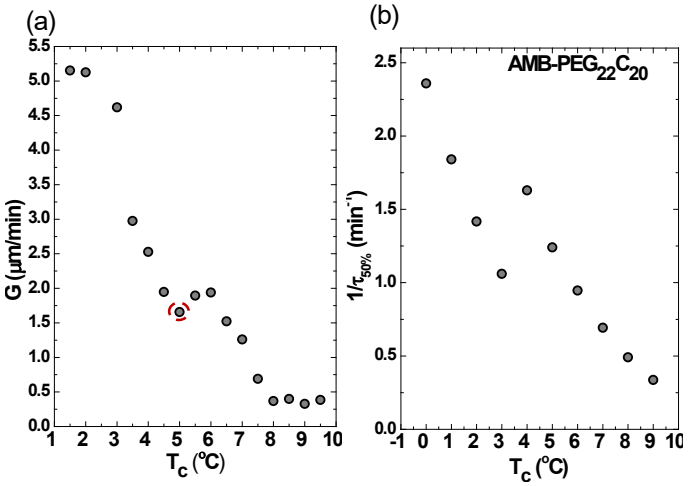

Figure 7. (a) Linear growth rate, G, of spherulites of AMB-PEG$_{22}$C$_{20}$ as a function of T$_c$, measured by PLOM. Isothermal protocol 1b: Cooling from the melt at 5 °C·min^{-1} to 10 °C, followed by further cooling from 10 °C at 50 °C·min^{-1} to the established crystallization temperature. (b) Experimentally determined overall crystallization rate ($1/\tau_{50\%}$) as a function of isothermal crystallization temperature. Isothermal protocol 1a: Cooling from the melt at 1 °C·min^{-1} to 10 °C, followed by further cooling from 10 °C at 50 °C·min^{-1} to the established crystallization temperature.

Furthermore, we performed isothermal crystallization experiments by DSC. These experiments take into account both primary nucleation and growth. The DSC experimental protocol employed is described in detail in the experimental part. The sample was cooled at 1 °C·min^{-1} to 10 °C to allow the crystallization of the alkyl chains to saturation. Then the sample was cooled at 50 °C·min^{-1} down to the T_c value, such fast cooling was employed to prevent the crystallization of the PEG side chains during cooling to T_c. Figure 7b shows a plot of overall crystallization rate (expressed as the inverse of the half-crystallization time)[54] as a function of crystallization temperature and Figure S7 shows the representative heat flow versus time plot. Remarkably, a similar minimum is observed in the overall crystallization rate, indicating that secondary nucleation (or growth) is the rate determining factor of the overall kinetics. The minimum occurs at slightly different temperature values (within 2 ºC), but given the fact that two techniques are involved, the values are close enough.

This distinct minimum in growth rate (and in overall crystallization rate) is analogous to observations in the crystallization rate of monodisperse long chain *n*-alkanes,[32,33] methyl-terminated low molecular weight poly(ethylene oxide) fractions,[55] and high molar mass polyethylenes with precision bromine pendant groups.[34] It was first explained, for both solution and melt crystallized systems, by Keller *et al.*[56,57] with the phenomenon termed *self-poisoning*. It was ascribed to the fact that chains incorrectly attached to the crystal surface may cause retardation in further crystal growth.[58] Whitelam *et al.*[59] recently presented a more general approach using dynamic mean-field theory and computer simulations to explain self-poisoning of crystal growth for any type of molecule. They postulated that *poisoning* is universal in any crystalline molecule provided the following physical aspects are met: (1) the molecule can attach in at least two different forms (optimal and non-optimal forms) to the crystal front, (2) the different forms are not

energetically equivalent and (3) the probabilities of binding to the crystal front for each form are significantly different.

With this in mind, it is important to reflect back on the architecture of our AMBs and the various aspects of its structure that may lead to frustration during the crystallization process. Firstly, the phase segregated AMBs contain PEG and alkyl side chains that are densely anchored on either side of an amorphous backbone. This may weaken the mobility of the side chains. Secondly, the presence of two different and crystallizable side chains, with different modes of packing, i.e., the hexagonal packing of icosane side chains and the helical structure with monoclinic cell in crystalline PEG may possibly frustrate the packing of the semicrystalline AMBs. Furthermore, DSC and WAXS measurements showed that the alkyl side chains crystallizes first followed by the PEG side chains. This ordering whereby the alkyl SCs are crystalline before the PEG side chains may add further constraints on the crystallization process of the PEG side chains, presumably leading to the observed minimum in crystallization rate.

SUMMARY AND CONCLUSIONS

In summary, a series of amphiphilic hetero-arm molecular brushes (AMBs) were easily prepared via *grafting through* using conventional FRP of monomers and macromonomers containing either PEG or alkyl chains of different lengths: hydrophilic 4-vinyl benzyl-(poly(ethylene glycol)) methyl ethers, tert-butyl diphenyl silyl poly(ethylene glycol) methacrylate, and hydrophobic *N*-alkyl maleimides. The thermal and structural behavior of these hAMBs featuring an amorphous main chain and densely packed crystallizable side chains were systematically investigated. DCS and X-Ray analysis revealed that side chain lengths, and possibly backbone rigidity affect the crystallization of PEG and alkyl side chains in the brush. AMBs with combinations of either low $D.P._{PEG}$, or short alkyl chain lengths, showed a more constrained

crystallization behavior, evidenced by lower degrees of crystallinity and were less able to form well-ordered structures, as revealed by SAXS analysis. The more constrained crystallization, in the other brushes, probably reduces the ability of the side chains of these brushes to be incorporated into growing adjacent crystalline lamellae, forcing them into the amorphous phase, further constraining crystal growth.

AMB-$PEG_{22}C_{20}$ was the only sample able to form spherulites (due to a break-out crystallization phenomenon or crystallization from a single phase melt) which could be visualized by PLOM. The PEG side chains spherulitic growth rate, as well as their overall crystallization rate, as a function of crystallization temperature, T_c, revealed anomalous minima, with increasing undercooling. Such minima are consistent with the self-poisoning effect observed with long chain n-alkanes, or high molar mass polyethylenes with precision bromine pendant groups. In this AMB-$PEG_{22}C_{20}$ case, we attribute the self-poisoning to frustration during crystallization caused by having to pack PEG side chains that are attached to the rigid amorphous main chain backbone that also contains previously crystallized alkyl side chains. This highlights the complexity of assembling such a material into a double crystalline form. This is the first such observation in hetero-arm molecular brushes.

ASSOCIATED CONTENT

The Supporting Information is available free of charge on the ACS Publications website.

Supporting Information. ^{1}H NMR spectra, DSC curves, WAXS/SAXS patterns and Avrami curves.

Corresponding Authors

*Email: rueben@sun.ac.za, alejandrojesus.muller@ehu.es, bklump@sun.ac.za

ORCID
Elaine Barnard: 0000-0002-1082-7074
Rueben Pfukwa: 0000-0002-4816-2848
Jon Maiz: 0000-0003-1942-1123
Alejandro J. Müller: 0000-0001-7009-7715
Bert Klumperman: 0000-0003-1561-274X

ACKNOWLEDGEMENTS

This work is based on the research supported by the South African Research Chairs Initiative of the Department of Science and Technology (DST) and National Research Foundation (NRF) of South Africa (Grant No 46855). J.M. acknowledges support from the Provincial Council of Gipuzkoa under the program Fellow Gipuzkoa and "Fomento San Sebastián" in the framework program "Retorno del Talento Local" Donostia up! 2016. This work has received funding from the European Union´s Horizon 2020 research and innovation program under the Marie Sklodowska-Curie grant agreement No 778092, from MINECO, project: MAT2017-83014-C2-1-P and from the Basque Government through grant IT1309-19. We also thank ALBA Synchrotron facility for providing funding and beam time (proposal number: 2018082953).

REFERENCES

1. Paquet, C. & Kumacheva, E. Nanostructured polymers for photonics. *Mater. Today* **11,** 48–56 (2008).

2. Acikgoz, C., Hempenius, M. A., Huskens, J. & Vancso, G. J. Polymers in conventional and alternative lithography for the fabrication of nanostructures. *Eur. Polym. J.* **47,** 2033–2052 (2011).

3. Son, D. & Bao, Z. Nanomaterials in Skin-Inspired Electronics: Towards Soft and Robust

Skin-like Electronic Nanosystems. *ACS Nano* **12,** 11731–11739 (2018).

4. Yadav, H. K. S., Almokdad, A. A., Sumia, I. M. & Debe, M. S. in *Nanocarriers for Drug Delivery* (eds. Mohapatra, S. S., Ranjan, S., Dasgupta, N., Mishra, R. K. & Thomas, S.) 531–556 (Elsevier Inc., 2019). doi:10.1016/B978-0-12-814033-8.00017-5

5. Patra, J. K. *et al.* Nano based drug delivery systems:recent developments and future prospects. *J. Nanobiotechnology* **16,** 1–33 (2018).

6. Mcdonald, T. O. *et al.* in *Nanoengineering* (ed. DOLEZ, P. I.) 173–223 (Elsevier B.V., 2015). doi:10.1016/B978-0-444-62747-6.00007-5

7. Wang, G., Morrin, A., Li, M., Liu, N. & Luo, X. Nanomaterial-doped conducting polymers for electrochemical sensors and biosensors. *J. Mater. Chem. B* **6,** 4173–4190 (2018).

8. Chem, J. M., Su, S., Wu, W., Gao, J. & Fan, C. Nanomaterials-based sensors for applications in environmental monitoring. *J. Mater. Chem.* **22,** 18101–18110 (2012).

9. Shi, H., Zhao, Y., Dong, X., Zhoua, Y. & Wang, D. Frustrated crystallisation and hierarchical self-assembly behaviour of comb-like polymers. *Chem. Soc. Rev.* **42,** 2075–2099 (2013).

10. Verduzco, R., Li, X., Pesek, L. & Stein, G. E. Structure, function, self-assembly, and applications of bottlebrush copolymers. *Chem. Soc. Rev.* **44,** 2405–2420 (2015).

11. Runge, M. B. & Bowden, N. B. Synthesis of High Molecular Weight Comb Block Copolymers and Their Assembly into Ordered Morphologies in the Solid State. *J. Am. Chem. Soc.* **129,** 10551–10560 (2007).

12. Xia, Y., Olsen, B. D., Kornfield, J. A. & Grubbs, R. H. Efficient Synthesis of Narrowly Dispersed Brush Copolymers and Study of Their Assemblies : The Importance of Side Chain Arrangement. *J. Am. Chem. Soc.* **131,** 18525–18532 (2009).

13. Ishizu, K. Architecture of Multi-Component Copolymer Brushes:Synthesis, Solution Properties and Application for Nanodevices. *Polym. J.* **36,** 775–792 (2004).

14. Atanase, L. I., Desbrieres, J. & Riess, G. Progress in Polymer Science Micellization of synthetic and polysaccharides-based graft copolymers in aqueous media. *Prog. Polym. Sci.* **73,** 32–60 (2017).

15. Rzayev, J. Molecular Bottlebrushes : New Opportunities in Nanomaterials. *ACS Macro Lett.* **1,** 1146–1149 (2012).

16. Li, J. *et al.* Phase Transition and Side-Chain Crystallization of Poly (methyl vinyl ether-alt-maleic anhydride)-g-Alkyl Alcohol Comb-like Polymers. *Macromolecules* **51,** 8922–8931 (2018).

17. Shi, H. *et al.* Effect of Main-Chain Rigidity on the Phase Transitional Behavior of Comblike Polymers. *Macromolecules* **40,** 3198–3203 (2007).

18. Sheiko, S. S., Sumerlin, B. S. & Matyjaszewski, K. Cylindrical molecular brushes: Synthesis, characterization and properties. *Prog. Polym. Sci.* **33,** 759–785 (2008).

19. Verduzco, R., Li, X., Pesek, S. L. & Stein, G. E. Structure, function, self-assembly, and applications of bottlebrush copolymers. *Chem. Soc. Rev.* **44,** 2405–2420 (2015).

20. Zhang, M. & Muller, A. H. E. Cylindrical polymer brushes. *J. Polym. Sci. Part A Polym.*

Chem. **43,** 3461–3481 (2005).

21. Xie, M. *et al.* Well-Defined Brush Copolymers with High Grafting Density of Amphiphilic Side Chains by Combination of ROP , ROMP , and ATRP. *Macromolecules* **41,** 9004–9010 (2008).

22. Neugebauer, D. *et al.* Densely Heterografted Brush Macromolecules with Crystallizable Grafts . Synthesis and Bulk Properties. *Macromolecules* **39,** 584–593 (2006).

23. Hu, M., Xia, Y., Mckenna, G. B., Korn, J. A. & Grubbs, R. H. Linear Rheological Response of a Series of Densely Branched Brush Polymers. *Macromolecules* **44,** 6935–6943 (2011).

24. Vlcek, P. *et al.* Bottlebrush-Shaped Copolymers with Cellulose Diacetate Backbone by a Combination of Ring Opening Polymerization and ATRP. *J. Polym. Sci. Part A Polym. Chem.* **46,** 564–573 (2007).

25. Zhu, H., Deng, G. & Chen, Y. Amphiphilic polymer brushes with alternating PCL and PEO grafts through radical copolymerization of styrenic and maleimidic macromonomers. *Polymer (Guildf).* **49,** 405–411 (2008).

26. Neugebauer, D. Graft copolymers with hydrophilic and hydrophobic polyether side chains. *Polymer (Guildf).* **48,** 4966–4973 (2007).

27. Stephan, T., Muth, S. & Schmidt, M. Shape Changes of Statistical Copolymacromonomers: From Wormlike Cylinders to Horseshoe- and Meanderlike Structures. *Macromolecules* **35,** 9857–9860 (2002).

28. Hattori, G., Hirai, Y., Sawamoto, M. & Terashima, T. Self-assembly of PEG/dodecyl-graft

amphiphilic copolymers in water: consequences of the monomer sequence and chain flexibility on uniform micelles. *Polym. Chem.* **8,** 7248–7259 (2017).

29. Xia, N. *et al.* Dynamically confined crystallization in a soft lamellar space constituted by alternating polymer co-brushes. *Polymer (Guildf).* **52,** 4581–4589 (2011).

30. Hattori, G. *et al.* Nanostructured Materials via the Pendant Self-Assembly of Amphiphilic Crystalline Random Copolymers. *J. Am. Chem. Soc.* **140,** 8376–8379 (2018).

31. Sun, H. *et al.* Configurationally Constrained Crystallization of Brush Polymers with Poly(ethylene oxide) Side Chains. *Macromolecules* **52,** 592–600 (2019).

32. Organ, S. J., Ungar, G. & Keller, A. Rate minimum in solution crystallization of long paraffins. *Macromolecules* **22,** 1995–2000 (1989).

33. Organ, S. ., Keller, A., Hikosaka, M. & Ungar, G. Growth and nucleation rate minima in long n-alkanes. *Polymer (Guildf).* **37,** 2517–2524 (1996).

34. Zhang, X., Zhang, W., Wagener, K. B., Boz, E. & Alamo, R. G. Effect of Self-Poisoning on Crystallization Kinetics of Dimorphic Precision Polyethylenes with Bromine. *Macromolecules* **51,** 1386–1397 (2018).

35. Hadasha, W., Mothunya, M., Akeroyd, N. & Klumperman, B. Synthesis and Self-assembly of Amphiphilic Hetero-arm Molecular Brushes. *Aust. J. Chem.* **64,** 1100–1105 (2011).

36. Zhu, J., Lines, B. M., Ganton, M. D., Kerr, M. A. & Workentin, M. S. Efficient Synthesis of Isoxazolidine-Tethered Monolayer-Protected Gold Nanoparticles (MPGNs) via 1,3-Dipolar Cycloadditions under High-Pressure Conditions. *J. Org. Chem.* **73,** 1099–1105

(2008).

37. Gembus, V., Marsais, F. & Levacher, V. An Efficient Organocatalyzed Interconversion of Silyl Ethers to Tosylates Using DBU and p -Toluenesulfonyl Fluoride. *Synlett* **10,** 1463–1466 (2008).

38. Zhang, Z. *et al.* One-pot synthesis of well-defined amphiphilic alternating copolymer brushes based on POSS and their self-assembly in aqueous solution. *RSC Adv.* **5,** 21580–21587 (2015).

39. Dodgson, K. & Ebdon, J. R. The Terpolymerisation of Styrene, Methyl Methacrylate and Maleic Anhydride. *Macromol. Chem.* **180,** 1251–1256 (1979).

40. Wang, H. *et al.* Structure and thermal performance of poly (styrene-co-maleic anhydride)-g-alkyl alcohol comb-like copolymeric phase change materials. *Thermochem. Acta* **564,** 34–38 (2013).

41. Arndtb, T., Schouten, A. J., Schmidtd, G. E. & Wegner, G. Langmuir-Blodgett mono- and multilayers of preformed poly(octadecyl methacrylates)s. Structural studies by IR spectroscopy and small-angle X-ray scattering. *Makromolecular Chem.* **192,** 2215–2229 (1991).

42. Xu, H., Gao, Y., Li, J., Wang, H. & Shi, H. Thermal performance and phase transformation of S-alkylated poly (vinyl chloride) comb-like polymers. *Polymer (Guildf).* **153,** 362–368 (2018).

43. Martuscew, E., Silvestre, C. & Gkrnondi, C. Morphology, crystallization and thermal behaviour of poly(ethylene oxide)/poly(vinyl acetate) blends. *Makromolecular Chem.* **186,**

2161–2176 (1985).

44. Wunderlich, B. in *Thermal Analysis of Polymeric Materials* 777–894 (1994).

45. Takahashi, Y. & Tadokoro, H. Structural Studies of Polyethers. X.Crystal Structure of Poly(ethylene oxide). *Macromolecules* **6,** 672–675 (1973).

46. Yao, N. Waxs studies on crystalline behavior of polymethyl methacrylate-polyethylene oxide graft copolymers and their ionic complexes. *J. Macromol. Sci. Part B* **30,** 225–243 (1991).

47. Inomata, K., Sakamaki, Y., Nose, T. & Sasaki, S. Solid-state structure of comb-like polymers having n-octadecyl side chains I. Cocrystallization of side chain with n-octadecanoic acid. *Polym. J.* **28,** 986–991 (1996).

48. Inomata, K., Sakamaki, Y., Nose, T. & Sasaki, S. Solid-State Structure of Comb-Like Polymers Having n-Octadecyl Side Chains II. Crystalline-Amorphous Layered Structure. *Polym. J.* **28,** 992–999 (1996).

49. Mark, P. R. *et al.* Microphase separated structures in the solid and molten states of double-crystal graft copolymers of polyethylene and poly (ethylene oxide). *Polymer (Guildf).* **49,** 3116–3124 (2008).

50. Sun, L., Liu, Y., Zhu, L., Hsiao, B. S. & Avila-Orta, C. A. Pathway-dependent melting in a low-molecular-weight polyethylene-block- poly(ethylene oxide) diblock copolymer. *Macromol. Rapid Commun.* **25,** 853–857 (2004).

51. Leibler, L. Theory of Microphase Separation in Block Copolymers. *Macromolecules* **13,**

1602–1617 (1980).

52. Castillo, R. V & Müller, A. J. Crystallization and morphology of biodegradable or biostable single and double crystalline block copolymers. *Prog. Polym. Sci.* **34,** 516–560 (2009).

53. Michell, R.M & Müller, A. J. Confined crystallization of polymeric materials. *Prog. Polym. Sci.* **54-55,** 183–213 (2016).

54. Lorenzo, A. T., Arnal, L., Albuerne, J. & Muller, A. J. DSC isothermal polymer crystallization kinetics measurements and the use of the Avrami equation to fit the data:Guidelines to avoid common problems. *Polym. Test.* **26,** 222–231 (2007).

55. Cheng, S. Z. D., Chen, J., Zhang, A. & Heberer, D. P. Nonintegral and integral folding crystal growth in low-molecular mass poly (ethylene oxide) fractions. II. End-group effect: α,ω-methoxy-poly (ethylene oxide). *J. Polym. Sci. Part B Polym. Phys.* **29,** 299–310 (1991).

56. Keller, A. & Avenue, T. Inversion of the temperature dependance of crystallization rates due to onset of chain folding. *Polymer (Guildf).* **28,** 1899–1907 (1987).

57. Organ, S. J., Ungar, G. & Keller, A. Rate Minimum in Solution Crystallization of Long Paraffins. *Macromolecules* **22,** 1995–2000 (2000).

58. Ungar, G., Putra, R., de Silva, D. S. ., Shcherbina, M. & Waddon, A. J. The Effect of Self-Poisoning on Crystal Morphology and Growth Rates. *Adv. Polym. Sci.* **180,** 45–87 (2005).

59. Whitelam, S., Dahal, Y. R. & Schmit, J. D. Minimal physical requirements for crystal growth self-poisoning. *J. Chem. Phys.* **144,** 064903 (2016).